Optical and X-ray GRB Fundamental Planes as Cosmological Distance Indicators

Dainotti, M. G.,[1,2,3]★ Nielson, V.[4,5] Sarracino, G.,[6,7] Rinaldi, E.,[8,9,10] Nagataki, S.,[11,10] Capozziello, S.,[6,7,12] Gnedin, O. Y.[5] and Bargiacchi, G., [7,12]

[1]National Astronomical Observatory of Japan, 2 Chome-21-1 Osawa, Mitaka, Tokyo 181-8588, Japan
[2]The Graduate University for Advanced Studies, SOKENDAI, Shonankokusaimura, Hayama, Miura District, Kanagawa 240-0193, Japan
[3]Space Science Institute, Boulder, CO, USA
[4]SLAC National Accelerator Laboratory, 2575 Sand Hill Road, Menlo Park, CA 94025, USA
[5]Astronomy Department, University of Michigan, Ann Arbor, MI 48109, USA
[6]Dipartimento di Fisica, "E. Pancini" Università "Federico II" di Napoli, Compl. Univ. Monte S. Angelo Ed. G, Via Cinthia, I-80126 Napoli (Italy)
[7]INFN Sez. di Napoli, Compl. Univ. Monte S. Angelo Ed. G, Via Cinthia, I-80126 Napoli (Italy)
[8]Physics Department, University of Michigan, Ann Arbor, MI 48109, USA
[9]RIKEN Cluster for Pioneering Research, Theoretical Quantum Physics Laboratory, 2-1 Hirosawa, Wako, Saitama, Japan 351-0198
[10]Interdisciplinary Theoretical & Mathematical Science Program, RIKEN (iTHEMS), 2-1 Hirosawa, Wako, Saitama, Japan 351-0198
[11]RIKEN Cluster for Pioneering Research, Astrophysical Big Bang Laboratory (ABBL), 2-1 Hirosawa, Wako, Saitama, Japan 351-0198
[12]Scuola Superiore Meridionale, Università di Napoli Federico II Largo San Marcellino 10, 80138 Napoli (Italy)

Accepted 2022 April 19. Received 2022 April 19; in original form 2021 December 1

ABSTRACT

Gamma-Ray Bursts (GRBs), can be employed as standardized candles, extending the distance ladder beyond Supernovae Type Ia (SNe Ia, $z = 2.26$). We standardize GRBs using the 3D fundamental plane relation (the Dainotti relation) among the rest-frame end time of the X-ray plateau emission, its corresponding luminosity, and the peak prompt luminosity. Combining SNe Ia and GRBs, we constrain $\Omega_M = 0.299 \pm 0.009$ assuming a flat ΛCDM cosmology with and without correcting GRBs for selection biases and redshift evolution. Using a 3D optical Dainotti correlation, we find this sample is as efficacious in the determination of Ω_M as the X-ray sample. We trimmed our GRB samples to achieve tighter planes to simulate additional GRBs. We determined how many GRBs are needed as standalone probes to achieve a comparable precision on Ω_M to the one obtained by SNe Ia only. We reach the same error measurements derived using SNe Ia in 2011 and 2014 with 142 and 284 simulated optical GRBs, respectively, considering the errorbars on the variables halved. These error limits will be reached in 2038 and in 2047, respectively. Using a doubled sample (obtained by future machine learning approaches allowing a lightcurve reconstruction and the estimates of GRB redhifts when z is unknown) compared to the current sample, with errorbars halved we will reach the same precision as SNe Ia in 2011 and 2014, now and in 2026, respectively. If we consider the current SNe precision, this will be reached with 390 optical GRBs by 2054.

Key words: gamma-ray burst: general; supernovae: general; cosmological parameters

1 INTRODUCTION

The tension on the Hubble constant cosmological parameter between different measurements is at the center of the debate in the astronomical and cosmological communities, and asks for a firm theoretical background at fundamental level (Capozziello et al. 2020; Dainotti et al. 2021e, 2022c). Using the Planck satellite to study the Cosmic Microwave Background (CMB) Radiation, distance measurements have been performed to derive the Hubble constant, H_0, with a very high precision. The same measurements have been used to derive the matter content of the Universe today, Ω_M. However, discrepancies in the range between $4-6\,\sigma$ in H_0 arise when we compare the measurements of these quantities by the CMB, an early Universe probe, with those obtained by Supernovae Ia (SNe Ia), or other late Universe probes, such as Cepheids. For years, SNe Ia have been studied and used as standard candles, because their nearly uniform luminosities (absolute magnitude M ≃ -19, Carroll (2001)) allow us to use them as reliable cosmological tools. Although they reach higher redshifts than other standard candles such as Cepheid Variables (Riess et al. 2021) and the Tip of the Red Giant Branch (TRGB, Chen et al. (2017); Abbott et al. (2018); Beaton & Carnegie-Chicago Hubble Program Team (2018); Birrer et al. (2020); Efstathiou (2020); Freedman et al. (2020); Cao et al. (2021b); Freedman (2021); Khetan et al. (2021); Lin & Ishak (2021)), which are the previous step in the so-called cosmological

ladder, they have still only been observed up to $z = 2.26$ (Rodney et al. 2015). Although there are also many groups that find lower H_0 values with larger error bars from low-z data that are reasonably consistent with the Planck 2018 value (Chen et al. 2017; Abbott et al. 2018; Birrer et al. 2020; Efstathiou 2020; Cao et al. 2021b; Freedman 2021; Khetan et al. 2021; Lin & Ishak 2021), to further try to resolve the issue of the Hubble tension, it is crucial to develop new cosmological probes at high-z to test cosmological models even further. If we consider an evolutionary trend existing in the SNe Ia data as it has been shown in Dainotti et al. (2021e, 2022c), we may bridge the gap among these probes by employing additional, *standardizable* candles that can be detected at high redshifts: Gamma-Ray Bursts (GRBs) and possibly quasars (QSOs) (Lusso et al. 2020; Bargiacchi et al. 2021).

For the use of GRBs as cosmological tools, one of the correlations that can be employed to make them a standardizable candle is the fundamental plane relation between the peak prompt luminosity, the rest-frame end time of the plateau, and its corresponding luminosity. In this work we do include a SNe Ia sample, although solely in conjunction with GRBs rather than as a calibrator. In the case of GRBs, there have been many attempts to use them as standard candles through a series of relationships among the prompt emission, the main explosion in γ-rays, and in its counterpart in X-rays and optical. The caveat in the use of the quasars with the Risaliti-Lusso relation is that selection biases in this correlation have only been addressed very recently (Dainotti et al. 2022a). These results show that this correlation is indeed intrinsic to the QSO physics and it is not due to selection biases, but it undergoes redshift evolution. Thus, these evolutionary effects need to be taken into account for the application of quasars-cosmology. Further, there is an ongoing discussion on the use of this correlation at high-z (beyond $z = 1.5$) and its effectiveness; for details see Khadka & Ratra (2021a,b).

Specifically, the application of GRBs as cosmological tools is worthwhile because they have been detected up to redshift $z = 9.4$ (Cucchiara et al. 2011), and in principle, they can be detected up to $z = 20$ (Lamb 2003). Other cosmological probes cannot be seen so far away; even the record-setting quasar J0313-1806, discovered very recently, reaches up to only $z = 7.642$ (Wang et al. 2021b). Thus, GRBs have fascinated the astrophysical community ever since their initial detection, and several attempts have been made to use them as cosmological tools or distance estimators (Amati et al. 2008; Capozziello & Izzo 2008, 2010; Kodama et al. 2008; Dainotti et al. 2011b; Demianski et al. 2012; Wang et al. 2016; Demianski et al. 2017a,b; Luongo & Muccino 2020). However, this is a complex task as GRBs are not yet standard candles in the sense that their observed luminosities vary greatly from one another. This issue regarding the heterogeneity of GRB luminosities remains an open topic due to the ambiguous nature of their origins. Certain types of GRBs may originate from the core collapse of a very massive star, as described by the "collapsar model" (Woosley 1993; Paczyński 1998; MacFadyen & Woosley 1999; MacFadyen et al. 2001), while other types may arise from the merger of two neutron stars (NS) in a binary system, or a NS–black hole (BH) system merger.

Studies are further complicated given the existence of many classes of GRBs. The scientific community began to categorize these objects by adopting the short and long GRB identifications based on the duration of their prompt emission, T_{90}, which indicates the time over which a burst emits 5% to 95% of its total measured counts (Mazets et al. 1981; Kouveliotou et al. 1993; Bromberg et al. 2013; Lü et al. 2014). Short GRBs (SGRBs) are defined by $T_{90} \leq 2$s, whereas long GRBs (LGRBs) have a $T_{90} > 2$s. However, in recent years, the Neil Gehrels Swift Observatory (hereafter Swift) has detected a subsequent phase following the prompt emission referred to as the afterglow phase. Furthermore, Swift has seen that 60% of GRB light curves (LCs) Dainotti et al. (2020a, 2021c) present a plateau in the afterglow emission followed by a power-law (PL) decay phase, as pinpointed by O'Brien & Willingale (2007); Sakamoto et al. (2007); Willingale et al. (2007); Tang et al. (2019); Zhao et al. (2019). Due to these added details, the two large classes of SGRBs and LGRBs have been scrutinized into many subclasses: X-ray flashes (XRFs) which have greater X-ray fluence ($2 - 30$ keV) than γ-ray fluence ($30 - 400$ keV), X-ray rich (XRR) which have the ratio of the X-ray fluence over the γ-ray fluence ranging to values peculiar to the regular GRBs and the XRFs, GRB-SNe Ib/c associated (SNe-GRBs), ultra-long GRBs (ULGRBs) with $T_{90} > 2000$ s (Gendre et al. 2013; Piro et al. 2014; Levan 2017), and short GRBs with extended emission (SEEs, Norris & Bonnell (2006); Levan et al. (2007); Norris et al. (2010)) which are characterized by mixed features between SGRBs and LGRBs. SEEs are harder in the spectrum than LGRBs, similarly to SGRBs, while intrinsically short (IS) GRBs have $T_{90}/(1 + z) < 2$ s. The underlying physical differences between sub-classes are still not completely understood, but are hypothesized to come from different GRB progenitors or diverse environments, such as either a constant interstellar medium (ISM) or a wind medium (Dainotti et al. 2021c). A more recent interpretation involves the sorting of these sub-classes into a different classification system based on previously proposed GRB progenitor physics that can be deduced by phenomenological and physical features (Zhang et al. 2006); Type I GRBs occur when two compact objects collide, and Type II emerge from massive star collapse. LGRB, XRF, XRR, SNe-GRB and ULGRB afterglow observations are usually consistent with the Type II-defined origins. SGRBs, SEEs, and IS GRBs are similarly ascribed within the Type I-defined origins. Still, there are some exceptions that do not allow us to match the two broad classifications exactly; for instance, some SGRBs have actually been classified as Type II (Zhang et al. 2009). In this study, we use a subclass of a well-defined sample of Type II GRBs from Swift (with z-range of $0.34 - 5.91$) as a cosmological tool through a well-established correlation involving properties of the plateau emission.

Regarding the use of GRBs as cosmological tools, before the launch of Swift, Amati et al. (2002a) analyzed a small sample of 12 GRBs collected by Beppo-SAX (Boella et al. 1997). They observed correlations that eventually led to their use as cosmological tools through the two-dimensional $E_p - E_{iso}$ relation (the so-called Amati relation, Amati et al. (2002b, 2008)), where E_p is the peak of $\nu F(\nu)$ spectrum, and E_{iso} is the isotropic energy of the prompt emission. Another prompt correlation has been discovered between $E_p - L_p$, where L_p is the isotropic peak luminosity of the prompt emission (Yonetoku et al. 2004). A similar correlation between the collimated-corrected energy ν and the peak flux in the spectrum F_ν has been determined by Ghirlanda et al. (2004) for a slightly larger sample of 40 pre-Swift GRBs. Yet another correlation seen shortly thereafter is the Liang & Zhang (2005) relation between E_p, E_{iso}, and the break time of the optical afterglow LCs, t_b. All of these relations are focused on the prompt emission properties. Thus, they have all also been employed in conjunction with SNe Ia data in attempts to constrain several cosmological parameters, such as H_0, Ω_M, and the dark energy parameter w.

After the launch of Swift and the addition of many higher-quality GRB detections, some of these aforementioned relations suffered increased scatter and became less reliable (Campana et al. 2007; Kocevski & Butler 2007). A novelty in the application of GRBs as cosmological tools is the use of correlations involving the plateau emission phase (Cardone et al. 2009, 2010; Dainotti et al. 2013a; Postnikov et al. 2014). The advantage of using correlations concerning the afterglow phase is that there exists less variability in its features compared to those of the prompt emission phase. In this paper, we leverage the plateau emission properties and use a tight multi-dimensional relation built using Swift GRBs presenting a plateau with known redshift (Dainotti et al. 2008). The 2D correlation between the X-ray rest-frame end time of the plateau $T_{a,X}$ and its corresponding luminosity $L_{a,X}$ defines the so-called Dainotti relation (Dainotti et al. 2008) that has been used to study and standardize GRB luminosities. This relation has been extensively confirmed in the following works: Dainotti et al. (2011b, 2013a, 2015b); Del Vecchio et al. (2016); Dainotti et al. (2017b). The discovery of the 2D Dainotti relation in X-rays marked the first time an afterglow correlation had been used as a cosmological tool (Cardone et al. 2009, 2010; Dainotti et al. 2013b; Postnikov et al. 2014). The 2D correlation in X-rays has been interpreted within several models such as the accretion onto the black hole (Cannizzo & Gehrels 2009, 2010), as powered by a fast spinning neutron star (Rowlinson et al. 2013, 2014; Stratta et al. 2018; Cao et al. 2021a, 2022; Hu et al. 2021; Wang et al. 2021a; Xu et al. 2020) or as a modification of the microphysical parameters models (Leventis et al. 2014; Van Eerten 2014a,b; Varela et al. 2016) which consider jets viewed slightly off-axis (Beniamini et al. 2020). Although these works deal strictly with the Dainotti relation in X-ray, recently it has been found that there exists also a two-dimensional relationship in optical wavelengths for a sample of 102 GRBs between the optical rest-frame end time, T_{OPT}, and the optical luminosity at the end of the plateau, L_{OPT} (Dainotti et al. 2020b). An extension of the $L_{OPT} - T_{OPT}$ relation, obtained by adding the energy in the prompt emission, E_{iso}, has been investigated with a sample of 50 GRBs (Si et al. 2018). Other correlations in optical have been discussed, which could possibly be related to the optical 2D Dainotti relation (Oates et al. 2015, 2017). This correlation resembles, in its slope, the X-ray Dainotti luminosity-time relation, and it can be interpreted within the magnetar model as well (Rowlinson et al. 2014; Bernardini 2015; Gompertz et al. 2015; Lü et al. 2015; Rea et al. 2015; Knust et al. 2017; Rowlinson et al. 2017; Yu et al. 2017; Li et al. 2018). Other attempts have been made to investigate the prompt-afterglow correlations between the luminosity at the end of the plateau emission, $L_{a,X}$ and the peak prompt luminosity at 1 s ($L_{peak,X}$, Dainotti et al. (2011a, 2015b)).

Since these discoveries, a third correlated GRB parameter has been found in X-ray wavelengths, thus defining the now 3D X-ray Dainotti relation. The addition of the peak luminosity in the prompt emission, $L_{peak,X}$, yields a significant decrease in the intrinsic scatter with respect to the correspondent 2D correlation. A very precise plane with small intrinsic scatter in a three-dimensional space of ($\log T^*_{a,X}$, $\log L_{a,X}$, $\log L_{peak,X}$) is thus defined, and is known as the GRB *fundamental plane*. This more reliable X-ray correlation has also been extensively studied: Dainotti et al. (2016, 2017c, 2020a, 2021c,d); Srinivasaragavan et al. (2020). More precisely, in Dainotti et al. (2017c) it has been discussed that the fundamental plane relation is a tool for discriminating among several classes of GRBs. In Stratta et al. (2018), it has been given a reliable physical grounding by explaining it within the magnetar model. In Srinivasaragavan et al. (2020), the X-ray fundamental plane has been used as a tool to discriminate among several scenarios of slow or fast cooling in a wind or a constant interstellar medium. It has been shown that the GRBs observed by Fermi-LAT and detailed in the Second Fermi GRB Catalog (Ajello et al. 2019), which show the existence of the plateau in γ-rays, obey this correlation as well (Dainotti et al. 2021d).

It is relevant here to briefly discuss other attempts in the literature to use both the Amati and Dainotti correlations to probe the effectiveness of constraints by GRBs on other cosmological parameters as well. For example, Khadka & Ratra (2020); Khadka et al. (2021) validate the Amati relation among six different cosmological models and show that the results obtained by using only GRBs for the constraint of all of the associated cosmological parameters are consistent with those by baryon acoustic oscillations (BAOs) and SNe Ia. Further, the Dainotti relation (which this paper employs) has been used by Wang et al. (2021a) to constrain ΛCDM model parameters, and they present results consistent with the predictions of the flat ΛCDM model at high GRB redshifts. Hu et al. (2021) combine a SGRB sample with the Wang et al. (2021a) LGRB sample to further constrain both Ω_M and Ω_Λ using the Dainotti correlation. The results are again consistent with a flat ΛCDM model. More recently, Cao et al.

(2021a, 2022) have combined both Wang et al. (2021a) and Hu et al. (2021) GRB data sets alongside the Amati-correlated GRBs and the results are in agreement with the Hubble parameter (H(z)) and BAO data-derived constraints. Very recently, the 2D Dainotti relation has also been investigated in radio emission (Levine et al. 2022) and it holds with parameters that are compatible with X-rays and optical when we correct for selection biases and redshift evolution (Dainotti et al. 2021b).
Given this series of papers (9 since 2016 dealing with the X-ray fundamental plane relation, the 2D relation in optical, and selection biases) we believe we are now ready to use the fundamental plane in X-rays and optical wavelengths as a cosmological tool. In this paper we test, for the first time in this research field, the novel 3D optical correlation as the extension of the 3D X-ray fundamental plane as a cosmological tool, and check its applicability compared to that of the confirmed X-ray relation. The goal is to employ the fundamental plane as a mean to use GRBs in X-rays and optical as standard candles to constrain cosmological quantities, in analogy to what has been done with SNe Ia. One important question to answer is to what extent the precision on cosmological parameters can be increased by these new probes, alone as well as with SNe Ia.
We show in this paper how the 3D Dainotti correlation has achieved a comparable or smaller intrinsic scatter ($\sigma_{\rm int} = 0.20 \pm 0.06$) than the aforementioned attempts. In particular, we show the most updated scatter for the discussed alternative correlations: $\sigma = 0.41 \pm 0.03$ is achieved with the $E_{\rm p} - E_{\rm iso}$ correlation (Amati et al. 2019; Cao et al. 2021a). This scatter comes from the highest data quality compilation, which is the A118 compilation of Khadka & Ratra (2020); Khadka et al. (2021), based on Wang et al. (2016) and Fana Dirirsa et al. (2019). When the GRB sample is calibrated using H(z) data, $\sigma = 0.20 \pm 0.01$ is achieved using the same correlation. Furthermore, after correcting for the jet opening angle, the scatter is reported to be 0.09 (Ghirlanda et al. 2007). Even more recently, Wang et al. (2018) found a wider scatter for this correlation; a dispersion value is not explicitly given in this report, but the normalization parameter is shown to hold a very high error. Lastly, for the $E_{\rm p}$-$E_{\rm iso}$-$t_{\rm b}$ correlation, a dispersion equal to 0.15 has been found (Wang et al. 2018). The main advantage of our method over these is that the 3D correlation here proposed has already been corrected for both selection biases and redshift evolution (Dainotti et al. 2013a, 2015a, 2020a; Dainotti & Amati 2018) with the reliable statistical Efron & Petrosian (1992) method. This is contrary to other relationships which have not been corrected for such biases; see Collazzi et al. (2012) on this topic. For reviews on the topic of GRB correlation both in the prompt and afterglow emission see Grupe et al. (2013); Dainotti & Del Vecchio (2017); Dainotti et al. (2018); Dainotti (2019). Because our data is corrected in this manner, we can be sure that the correlation is intrinsic to the GRBs' physics and not due to selection biases.
The main goal of this work is to investigate the possibility of using GRBs as cosmological tools, together with SNe Ia as well as alone. To achieve this goal, we need to have the smallest possible scatter in the GRB fundamental plane correlation, given the difficulty in their standardization. To this end, we consider the data currently available, as well as data expected to be gathered in the next years by present and future deep-space observational missions and campaigns. In Sec.§2, we describe the GRB and SNe Ia data samples. In Sec.§3 we detail the calculations regarding $\Omega_{\rm M}$ and its error measurements. In Sec.§4 we present the results using the same methodology shown in Sec.§3, but considering a GRB sample in optical wavelengths. We perform redshift evolution and bias correction on all GRB samples in Sec.§5. We then describe the techniques used to simulate additional GRBs in X-ray and in optical to constrain $\Omega_{\rm M}$ with the same precision reached by the SNe Ia (Sec.§6), and define the minimum number of GRBs needed to do so at the end of Sec.§6.1. In Sec.§7 we use this number to define a timeline in which we will reach it through current and proposed deep-space satellite surveys. Finally, in Sec.§8, we abridge our findings and conclusions. In the Appendix Sec.§A, methods concerning the quantification of numerical Monte Carlo Markov Chain (MCMC) sampling error are discussed to assert the validity of our results. In the Appendix Sec.§B, we present more specific details on the sample selection process concerning the Sec.§6 simulations.

2 SAMPLE SELECTION FOR GRBS AND SNE IA

We select our X-ray GRB sample from an initial set of all 372 GRBs observed by Swift from 2005 January to 2019 August for which a redshift has been observed taken from Swift+BAT+XRT repository (Evans et al. 2009). From these, only those that are successfully fit by the Willingale et al. (2007) model and showing a reliable plateau are chosen. This reduces the starting sample to one of 222 GRBs. Furthermore, it is imperative to define phenomenological GRB categories to reach a reduction in the intrinsic scatter within this 3D relation. Thus, we focus only on the use of LGRBs from which XRFs, XRR, GRB-SNe Ib/c, and ULGRBs are removed. This is because Dainotti et al. (2016, 2017c, 2020a) have shown that the segregation in classes is essential for a) pinpointing a more homogeneous physical mechanism, and b) reducing the scatter of the correlation at the minimal point. Alongside these initial efforts to find a suitable sample, within the chosen LGRB class we also apply morphological criteria to the GRB LCs. This defines our final, "platinum" subsample, as also defined in Dainotti et al. (2020a), hereafter called the PLAT sample. To build this set, we have excluded the LCs of all the GRBs with at least one of the following features:

(i) an ill-defined onset point of the plateau phase, starting from its beginning;
(ii) an observed time at the end of the plateau, $T_{\rm a}$, that falls within a large observational gap;

Table 1. This table showcases the p-values for each variable achieved by the KS test when comparing the full population of GRBs to the chosen sampling distribution. The first row shows the p-values for the X-ray GRB parameters, and the second shows the same for the optical GRB parameters.

GRB Sample	KS(L_a)	KS(L_{peak})	KS(T_a^*)	KS(z)
X-ray	0.460	0.068	0.240	0.340
Optical	0.670	N/A	0.004	0.960

(iii) a short-duration plateau (< 500 s);
(iv) flares at anytime during the plateau phase;
(v) less than 5 observational points before the plateau phase;
(vi) an inclination of the plateau larger than 41°, similarly to what has been done in previous papers (Dainotti et al. 2016, 2017c, 2020a).

After these exclusions, a sample of 50 GRBs remains and defines our PLAT sample, with redshift range $0.055 < z < 5$. As a consequence of this choice, the PLAT fundamental plane will produce increasingly accurate estimates on cosmological parameters, and in this specific case, a better constraint on Ω_M. Regarding the optical data, we select all GRBs taken from Dainotti et al. (2020b), the GCN, and from private communication from Liang and Kann presenting both a plateau and a peak in the optical prompt emission (Dainotti et al. 2021 [in prep]). In total, these sources provide a full optical sample of 45 GRBs. Details of the data gathering and the selection and fitting criteria are presented in Dainotti et al. (2020b). The fitting procedure for determining the presence of the optical plateaus is again determined based on the phenomenological Willingale et al. (2007) function, as it was for the X-ray sample. In regards to a similar “platinum" trim for these optical LCs, we find that the optical sample so far is still too small to allow such scrutiny. Future analysis will allow us to increase the sample size and to uniformly use the definition of the platinum sample in optical too. Besides the morphological investigation, we account for biases in our selection process and redshift evolutionary effects using the Efron & Petrosian (1992) methodology, as it has been done in previous works (Lloyd 2000; Dainotti et al. 2013a, 2015a; Petrosian et al. 2015; Dainotti et al. 2020a).
Regarding the use of other cosmological probes in this study, our SNe Ia sample is the “Pantheon Sample" (PS) built by Scolnic et al. (2018); it is an aggregation of 1048 SNe Ia which ranges from $0.01 < z < 2.3$. It is worth noting that our 50 PLAT GRBs have been selected from a total number of 1305 GRBs observed by Swift from January 2005 up to 2019 August. In comparison, the PS has been slimmed down from a total of 3473 SNe Ia events from the full samples of each survey used in the catalogue. The total number of SNe Ia events is almost three times as large as the total number of GRBs. Our selection of the PLAT sample trims drastically the full data set to the 30% of the total sample, while the SNe Ia trims the sample of 4% (Scolnic et al. 2018).

2.1 Comparison of the X-ray and optical chosen samples vs the full X-ray and optical sample

We here show how much the properties of the X-ray and optical chosen samples are representative of population of GRBs if we select a sample composed of bright GRBs. Bright GRBs overcome the problem of selection biases because GRBs with a high luminosity will be less affected by the Malmquist bias effect (Malmquist 1922) induced by the missing population of faint events. Thus, we perform a cut in luminosity within the full X-ray GRB sample so that $\log L_{a,X} > 46.5$ erg s^{-1} and $\log L_{peak,X} > 49.5$ erg s^{-1}. These values do not change their respective luminosity functions significantly even if they are not corrected for selection biases (for details on the computation of the luminosity functions corrected for selection biases see Dainotti et al. (2013a); Petrosian et al. (2015)). To ensure that the PLAT sample is representative of the entire population, we perform the two-sample Kolmogorov–Smirnov (KS) test distribution of the $L_{a,X}$, $T^*_{a,X}$, and $L_{peak,X}$ of the PLAT sample. The resulting KS statistic highlights whether or not the two samples come from the same parent distribution. The cuts of $\log T^*_{a,X}/s = 1.76$ and $z = 0.54$ are performed so that we choose the sample to have plateaus which are not too short, so that there is no ambiguity on the existence of the plateau itself. Indeed, LCs with very small plateaus could be in principle compatible with a simple power law fit. We choose the minimum redshift of the PLAT sample. We perform the same comparison between the $L_{a,OPT}$, $T^*_{a,OPT}$ of the chosen sample versus the full sample of 181 optical LCs with plateaus. The cut for the full optical sample is $\log L_{a,OPT} = 43.5$ erg s^{-1}, $\log T^*_{a,OPT}s = 2.41$, and $z = 0.34$.
With these cuts in time, luminosity, and redshift, we then perform the KS test on each data set to compare the chosen samples used in this paper with respect to the full samples from which we have chosen them from. This test was performed on each aforementioned trimmed variable set, and the resulting p-values are shown in Table 1.
The KS test was performed with a null hypothesis stating that the underlying continuous distributions are identical. Before testing, we defined the p-value for which we will either reject or fail to reject the null hypothesis: $p = 0.05$. Table 1 shows that for all cases excluding the optical $T^*_{a,OPT}$ values, we fail to reject the null hypothesis and thus we can conclude that these chosen samples are indeed well representative of their populations. It is important to note first that there was no testing performed

on the $L_{\rm peak,OPT}$ values for the optical set because our chosen optical sample are only those GRBs whose $L_{\rm peak,OPT}$ have been measured, so there are no additional values of $L_{\rm peak,OPT}$ to be compared with. Our current chosen optical sample is the largest in the literature to date with $L_{\rm peak,OPT}$ measurements. Therefore, in noting the fact that we must reject the null hypothesis for the optical $T^*_{\rm a,OPT}$ values, it must be recognized that the optical sample is nevertheless the largest analyzed so far with current GRB data. In the near future, when additional analysis of new data is available we will be able to increase the chosen optical sample for the 3D correlation and thus overcome the differences in the rest-frame end-time population. We conclude that, with the current sample, all X-ray variables and optical luminosities are compatible with their respective parent populations.

3 DERIVING $\Omega_{\rm M}$ WITH THE FULL X-RAY GRB SAMPLE + SNE IA DATA

We begin this analysis using GRB emission data in X-ray in conjunction with SNe Ia data, utilizing the samples defined in the previous section. We here describe the methodology regarding the analysis of GRBs and SNe Ia to derive $\Omega_{\rm M}$ keeping H_0 fixed at $H_0 = 70$ km s^{-1}Mpc^{-1} and $w = -1$. In particular, we present the computations performed to derive this cosmological parameter by using the fundamental plane correlation built with the PLAT sample, both with and without the correction of selection biases and redshift evolution. First, we describe the GRB fundamental plane used in combination with the SNe Ia data. In all subsections below, the driving methodology is the same: we aim to find the best fitting three-dimensional coefficients of the fundamental plane together with the best fit value for $\Omega_{\rm M}$ using a Bayesian approach. We now start by describing the equation of the fundamental plane for a given fixed cosmological model. Later in our calculations, we vary $\Omega_{\rm M}$ together with the other fundamental plane variables. In order to build the likelihood pertaining to the GRBs, we start from the 3D Dainotti correlation which is described by the following equation:

$$\log_{10} L_{\rm a} = a \cdot \log_{10} T^*_{\rm a} + b \cdot \log_{10} L_{\rm peak} + c \tag{1}$$

where c is the normalization parameter, and a and b are the best fit scaling parameters for the PLAT sample, related to $\log_{10} T^*_{\rm a}$ and $\log_{10} L_{\rm peak}$, respectively. The equation above is general and is used for the other planes described in the paper. We here use different notations for the parameters according to the sample used, such as in X-rays or in optical or the full sample or trimmed. Here, $T^*_{\rm a,X}$ refers to the X-ray rest-frame end time of the plateau, and $L_{\rm a,X}$ refers to its corresponding luminosity. We retrieve these parameters $L_{\rm peak,X}$ and $L_{\rm a,X}$ by selecting directly from our sample LCs once they have been fit to the phenomenological Willingale et al. (2007) model. This model's functional form for a LC contains the parameters of the fluxes and times at the end of the plateau emission which do not depend on any assumption of a cosmological model nor SNe Ia calibration.

Bayesian, rather than frequentist, methods are utilized to derive precise estimates of the resulting fundamental plane parametric values. Specifically, we fit and compute all following parameters using the D'Agostini (D'Agostini 2005) method because it takes into account all variable uncertainties, both statistical and systematic, and it directly infers the intrinsic scatter. We here write a generic function for the likelihood that can be applied to any plane (X-rays, optical for the full sample and for a trimmed one). The fitting algorithm is defined by the following function of log-likelihood:

$$\mathcal{L}(a,b,c,\sigma_{\rm int}) = -\frac{1}{2}\cdot(ln(\sigma^2_{\rm int} + b^2\cdot\log^2_{10}(L_{\rm peak\ err}) + a^2\cdot\log^2_{10}(T^*_{\rm a\ err}) + \log^2_{10}(L_{\rm a\ err}))) - \frac{1}{2}\cdot\frac{(\log_{10}(L_{\rm a,th}) - \log_{10}(L_{\rm a}))^2}{\sigma^2_{\rm int} + b^2\cdot\log^2_{10}(L_{\rm peak\ err}) + a^2\cdot\log^2_{10}(T^*_{\rm a\ err}) + \log^2_{10}(L_{\rm a\ err})}, \tag{2}$$

where $T^*_{\rm a\ err}$, $L_{\rm peak\ err}$, and $L_{\rm a\ err}$ are the errors on the rest-frame time corresponding to the end of the plateau, the peak luminosity of the emission, and the luminosity at the end of the plateau, respectively, and $L_{\rm a,th}$ is the theoretically-computed luminosity at the end of the plateau as shown in Equation (1); $\sigma_{\rm int}$ is the intrinsic scatter on the plane which depends on an unknown source of scatter. To calculate a, b, c, and $\sigma_{\rm int}$, we make use of MCMC sampling. We use the python MCMC sampler *cobaya* (Torrado & Lewis 2019, 2021) to allow the plane parameters and the scatter of the plane to vary together. This is a crucial point in our methodology, since it avoids the so-called circularity problem. We also define very reasonable priors, so that we do not risk to incur in parameters which are not physically possible and not pertinent to the physical parameter space of the fundamental plane relation. The results we have obtained by using this method on the PLAT sample (denoted by 'X, PLAT' subscripts) are as follows: $a_{\rm X,PLAT} = -0.88 \pm 0.12$, $b_{\rm X,PLAT} = 0.55 \pm 0.12$, $c_{\rm X,PLAT} = 22.56 \pm 6.37$. The only assumption we make to derive these values is that the fundamental plane exists and is reliable along with its parameters. As computed for this plane, $\sigma_{\rm int_{X,PLAT}} = 0.36 \pm 0.04$. These results are visualized in Fig. 1 (upper left).

To use these relations for computing the best fit value for $\Omega_{\rm M}$, we begin by comparing the observed distance modulus, $\mu_{\rm obs,GRB}$, to the theoretical $\mu_{\rm theory}$ value. We first define the theoretical distance modulus:

$$\mu_{\rm theory} = 5\cdot\log_{10} d_{\rm L}(z, H_0, \Omega_{\rm M}) + 25, \tag{3}$$

where $d_{\rm L}$ is the luminosity distance, and z is redshift. Using a flat ΛCDM model, we define

$$\frac{H_z}{H_0} = \sqrt{\Omega_{\rm r}(1+z)^4 + \Omega_{\rm M}(1+z)^3 + \Omega_{\rm k}(1+z)^2 + \Omega_\Lambda} \tag{4}$$

where $\Omega_{\rm r}$ is the radiation energy density, the curvature of the Universe Ω_k is considered flat, and $H_0 = 70$ km s^{-1}Mpc^{-1}. We choose to neglect $\Omega_{\rm r}$ in our computations because the Universe seems to be closely represented by $\Omega_{\rm r} = 0$. Finally we define the theoretical luminosity distance as

$$d_{\rm L}(z, H_0, \Omega_{\rm M}) = (1+z)\frac{c}{H_0}\int_0^z \frac{dz'}{\sqrt{\Omega_{\rm M}(1+z')^3 + \Omega_\Lambda}} \tag{5}$$

where the dark energy density $\Omega_\Lambda = 1 - \Omega_{\rm M}$ given this flat cosmological model in the Friedmann Lemaitre Robertson Walker metric. Using this definition of luminosity distance, we hereby define the likelihood for the full GRB sample. We compare Equation (3) with the observed distance modulus that we can derive from the fundamental plane correlation in Equation (1), by isolating the luminosity distance in the following way:

$$\log_{10}(d_{\rm L}) = \frac{a\log_{10}T_{\rm a}^*}{2(1-b)} + \frac{b\cdot(\log_{10}F_{\rm peak} + \log_{10}K_{\rm peak})}{2(1-b)} + \frac{(b-1)\log_{10}(4\pi)+c}{2(1-b)} - \frac{\log_{10}F_{\rm a} + \log_{10}K_{\rm a}}{2(1-b)} \tag{6}$$

where $K_{\rm peak}$ and $K_{\rm a}$ are the K-corrections for cosmic expansion (Bloom et al. 2001) computed for the prompt and the afterglow, respectively. This relation was achieved by defining $L_{\rm a}$ as $4\pi d_L^2 F_{\rm a}$, with $F_{\rm a}$ as the flux at $T_{\rm a}^*$, and defining $L_{\rm peak}$ as $4\pi d_{\rm L}^2 F_{\rm peak}$, with $F_{textpeak}$ as the peak flux in the prompt emission. Using now the definition of the distance modulus and the new variables definitions $a_1 = a/(2(1-b))$; $b_1 = b/(2(1-b))$; $c_1 = ((b-1)\log_{10}(4\pi) + C)/(2(1-b))$; $d_1 = -1/(2(1-b))$; $F_{\rm peak,cor} = F_{\rm peak}\cdot K_{\rm peak}$; and $F_{\rm a,cor} = F_{\rm a}\cdot K_{\rm a}$, we obtain:

$$\mu_{\rm obs,\,GRB} = 5\cdot(a_1\ \log_{10}(T_{\rm a}^*) + b_1\ \log_{10}(F_{\rm peak,cor}) + c_1 + d_1\ \log_{10}(F_{\rm a,cor})) + 25. \tag{7}$$

This allows us to define the following likelihood that has the advantage to use the distance modulus directly, as the one related to SNe Ia does:

$$\mathcal{L}_{\rm GRB} = \sum_i \left(ln\left(\frac{1}{\sqrt{2\pi}\sigma_{\mu,i}}\right) - \frac{1}{2}\left(\frac{\mu_{\rm th,GRB,i} - \mu_{\rm obs,GRB,i}}{\sigma_{\mu,i}}\right)^2\right) \tag{8}$$

where $\sigma_{\mu,i}$ is the error on the observed distance moduli. The observed distance moduli obtained by the GRBs through the variables pertinent to the fundamental plane is compared with the theoretical GRB distance moduli. Specifically, the observed quantities of the GRBs do not depend on cosmology, since they are the observed flux, $F_{\rm a}$, its rest-frame time at the end of the plateau emission, $T_{\rm a}^*$ and the peak prompt flux, $F_{\rm peak}$. The parameters a_1, b_1 and c_1 are defined from a, b, and c which are left free to vary and converge to the theoretical distance of the GRBs. They are completely independent from the distance of the SNe Ia. We calculate the theoretical distance within large priors of $0 < \Omega_{\rm M} < 1$. The parameters that minimize the difference between the theoretical and observational moduli then provide the most probable values of $\Omega_{\rm M}$. We fix reasonable priors of the a, b and c and implicitly in a_1, b_1 and c_1 so that the parameters of the fundamental plane remain roughly constant in ranges compatible with the expected underlying physics of the correlation. By keeping these reasonable ranges the reliability of the plane is thus preserved. In this regard, GRBs through the fundamental plane relation can be considered standardizable candles because the parameters of the correlations are left to vary within physical allowed ranges. For example, we cannot allow the a parameter to be greater than zero, because it would then imply a different physics and as a consequence the energy reservoir of the plateau would not be constant (see the magnetar model for the evaluation of this parameter being closer to −1, (Stratta et al. 2018)). Similarly, we cannot allow the b parameters to be less than zero. This would not respect the physical observations that the more kinetic energy is transferred in the prompt, the more to the afterglow as it is demonstrated in Dainotti et al. (2017a, 2015b). This assumption is supported by theoretical modeling (Van Eerten 2014a,b).

We then also compare $\mu_{\rm theory}$ to the observed distance modulus of the SNe Ia sample, $\mu_{\rm obs,\,SNe}$, and finally compute the likelihood for the full sample. We add SNe Ia by allowing the total likelihood to encompass all samples:

$$\mathcal{L}_{\rm Tot} = \mathcal{L}_{\rm GRB} + \mathcal{L}_{\rm SNe} \tag{9}$$

where $\mathcal{L}_{\rm SNe}$ is the minimizing functions defined canonically for the SNe Ia sample:

$$\mathcal{L} = -\frac{1}{2}\sum_i \frac{(\mu_{\rm obs}^i - \mu_{\rm theory}^i)^2}{(\epsilon_{\mu_{\rm obs}}^i)^2}. \tag{10}$$

We generalize the above equation into

$$\mathcal{L} = -\frac{1}{2}\mathbf{\Delta\mu}^T \mathbf{C}^{-1}\mathbf{\Delta\mu} \tag{11}$$

where C is the covariance matrix, including both statistical uncertainties diagonally and systematic contributions in the opposed diagonal.

We now allow Ω_M to vary together with the fundamental plane parameters with a uniform prior in the interval $0 \leq \Omega_M \leq 1$. When we use this GRB sample in conjunction with the SNe Ia, we observe an $\Omega_M = 0.299 \pm 0.009$. Conversely, previous results for this cosmological parameter, probing only with SNe Ia data, yield an $\Omega_M = 0.298 \pm 0.008$. Slightly increased error bars on Ω_M exist due to the addition of the errors carried out from the GRB sample. However, we show in the following sections how the sample can be resized so that we can reduce the GRB scatter to produce the smallest error bars on Ω_M yet when we consider evolution (see Sec.§5).

3.1 Deriving Ω_M with the Trimmed X-ray GRB Sample + SNe Ia

To make the errors on the parameters computed in this analysis as small as possible, we now look for the tightest fundamental plane correlation by considering a subset of the X-ray PLAT sample composed of only the GRBs whose plane has an intrinsic scatter near zero. The goal is to reduce the error bars on Ω_M from what was computed before with SNe Ia + PLAT. This is done by calculating the closest GRBs to the X-ray fundamental plane. We choose this number to be 10 GRBs from the full PLAT sample, and hereby refer to this subsample as the trimmed platinum sample (PLATtrim). These 10 GRBs constitute a large enough sample to define a plane, yet still give a $\sigma_{\text{int}_{\text{X, trim}}}$ near zero. By increasing the sample, $\sigma_{\text{int}_{\text{X, trim}}}$ also increases. In these calculations, a near-zero intrinsic scatter is one on the order of 10^{-2} or smaller. In this section, we consider this new subsample of the X-ray GRBs using GRBs + SNe Ia to again derive Ω_M.

The results for this new plane fitting of the PLATtrim sample are as follows: $a_{\text{X,trim}} = -0.89 \pm 0.08$, $b_{\text{X, trim}} = 0.54 \pm 0.005$, $c_{\text{X, trim}} = 20.14 \pm 4.05$, and $\sigma_{\text{int}_{\text{X, trim}}} = 0.05 \pm 0.05$. These results are seen in Fig. 1 (upper right). By the trimming of the PLAT sample, we use this newly-defined fundamental plane for which a smaller intrinsic scatter exists in comparison to the full PLAT sample. Again, we perform cosmological computation together with SNe Ia data, and we obtain $\Omega_M = 0.299 \pm 0.009$. It should be noted that the errors on the uncertainties on Ω_M determined by the MCMC calculations are one order of magnitude less than the uncertainties on Ω_M itself; for details, see Appendix Sec. §A.

The full compilation of results are compared in Table 2. With the inclusion of the SNe Ia, we do not yet see an improvement in the results by the combination of probes by trimming the PLAT sample down to the 10 GRBs closest to the plane. The table makes clear that the PLATtrim sample has yet to be more efficacious in the reduction of the overall scatter, and consequently, in the error on Ω_M. We reach the same precision on Ω_M as the one obtained by the SNe Ia when the evolutionary parameters shown in Table 3 are considered (see Table 4). In Sec.§6, the true effects of the PLATtrim sample becomes visible and efficacious when we run simulations; the precise plane that the PLATtrim sample define is used successfully as a base for simulating additional GRBs.

As a final note, we must also stress that there is no calibration of the PLAT sample related to the SNe Ia, but we do fix the flat ΛCDM model to perform a comparison with the uncertainties derived with SNe Ia. However, it is important to note that the goal of the paper is to explore the reliability of the fundamental plane as a cosmological tool in comparison with SNe Ia, and not comparing different cosmological models. We additionally point out that this procedure of trimming the sample is meant to show how many GRBs should be used in the future once more data is available. This is the reason why the trimmed sample is the basis of our MCMC simulations and will inform us on how many of these GRBs close to the fundamental plane need to be chosen in order to have similar precision on the Ω_M parameter compared to the SNe Ia.

4 EXPLORING THE EFFICACY OF DERIVING Ω_M WITH OPTICAL GRB SAMPLES + SNE IA DATA

In this section, we shift from the use of the X-ray GRB emission data to test the reliability of optical GRB data. Similarly to the methodology used in the case of the X-ray fundamental plane, we calculate the number of GRBs closest to the optical plane that hold the intrinsic scatter to near-zero values. We investigate the 3D Dainotti relation at optical wavelengths to see how tight the plane is for a sample of 45 GRBs. The ability of this subsample to infer the parameters is then compared to that of the entire optical sample.

Once again using the D'Agostini methodology, we compute the 3D fundamental plane parameters and the correspondent intrinsic scatter of the full optical GRB sample. The results are the following: $a_{\text{OPT}} = -0.87 \pm 0.11$, $b_{\text{OPT}} = 0.37 \pm 0.08$, $c_{\text{OPT}} = 31.46 \pm 4.07$, and $\sigma_{\text{int}_{\text{OPT}}} = 0.53 \pm 0.04$, and are shown in Fig. 2 (upper left). Combining the full optical sample (OPT) with SNe Ia data, we obtain $\Omega_M = 0.299 \pm 0.009$ (Fig. 2, lower left). This analysis has been performed fixing the value of the

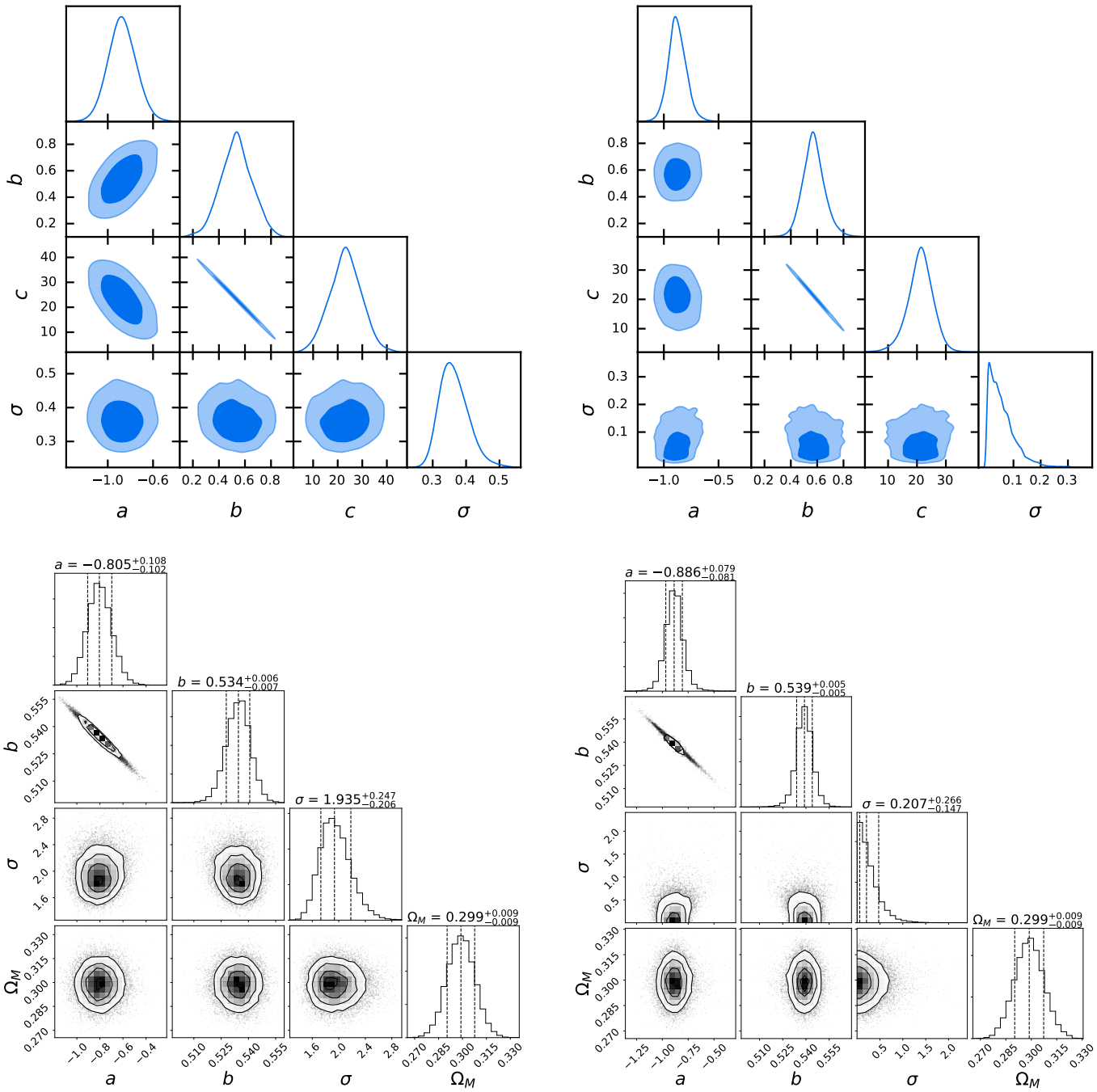

Figure 1. This figure compares the PLATtrim over PLAT when both are paired with SNe Ia data. The upper panels show the fundamental plane fitting for the full GRB PLAT sample (upper left) and the PLATtrim (upper right) calculated with *cobaya*. The bottom panels show the derivation of the Ω_M correspondent to the upper panels by the SNe Ia combined with both the full PLAT and PLATtrim samples. Each plot shows the 2D posterior contours.

parameter $c_{OPT} = 30$ following the same strategy of Amati et al. (2019). This result is novel and beneficial; the error is on par with that obtained by X-ray GRB samples. This means that the use of optical GRB samples may prove just as or perhaps more efficacious in constraining cosmological parameters with a future larger sample. This leads us to perform a similar trim on this optical data as to the one performed on the X-ray sample in an attempt to better understand the behavior of the optical data.

We find and consider only the optical GRBs closest to the plane with the aim to produce a sample with near-zero intrinsic scatter, hereby referred to as the optical trimmed sample (OPTtrim). We determine through testing that the maximum number of optical GRBs that maintain this level of accuracy is 10, as it was also in X-ray, and the best-fit results are as follows: $a_{OPT,trim} = -0.84 \pm 0.07$, $b_{OPT,trim} = 0.40 \pm 0.09$, $c_{OPT,trim} = 29.87 \pm 4.12$, and $\sigma_{int_{OPT,trim}} = 0.11 \pm 0.08$ (Fig. 2, upper right). Again, $\sigma_{int_{OPT,trim}}$ peaks around zero. We again include SNe Ia, resulting in an $\Omega_M = 0.299 \pm 0.009$ (Fig. 2, lower right). We here

Table 2. The first column refers to the sample used, while the second column refers to the results of Ω_M. Results are obtained without the correction for evolution. The errors reported in this table are the corresponding to the 68% confidence limit.

Sample	Ω_M
SNe	0.299 ± 0.008
PLAT+SNe Ia	0.299 ± 0.009
PLATtrim+SNe Ia	0.299 ± 0.009
OPT+SNe	0.299 ± 0.009
OPTtrim+SNe Ia	0.299 ± 0.009

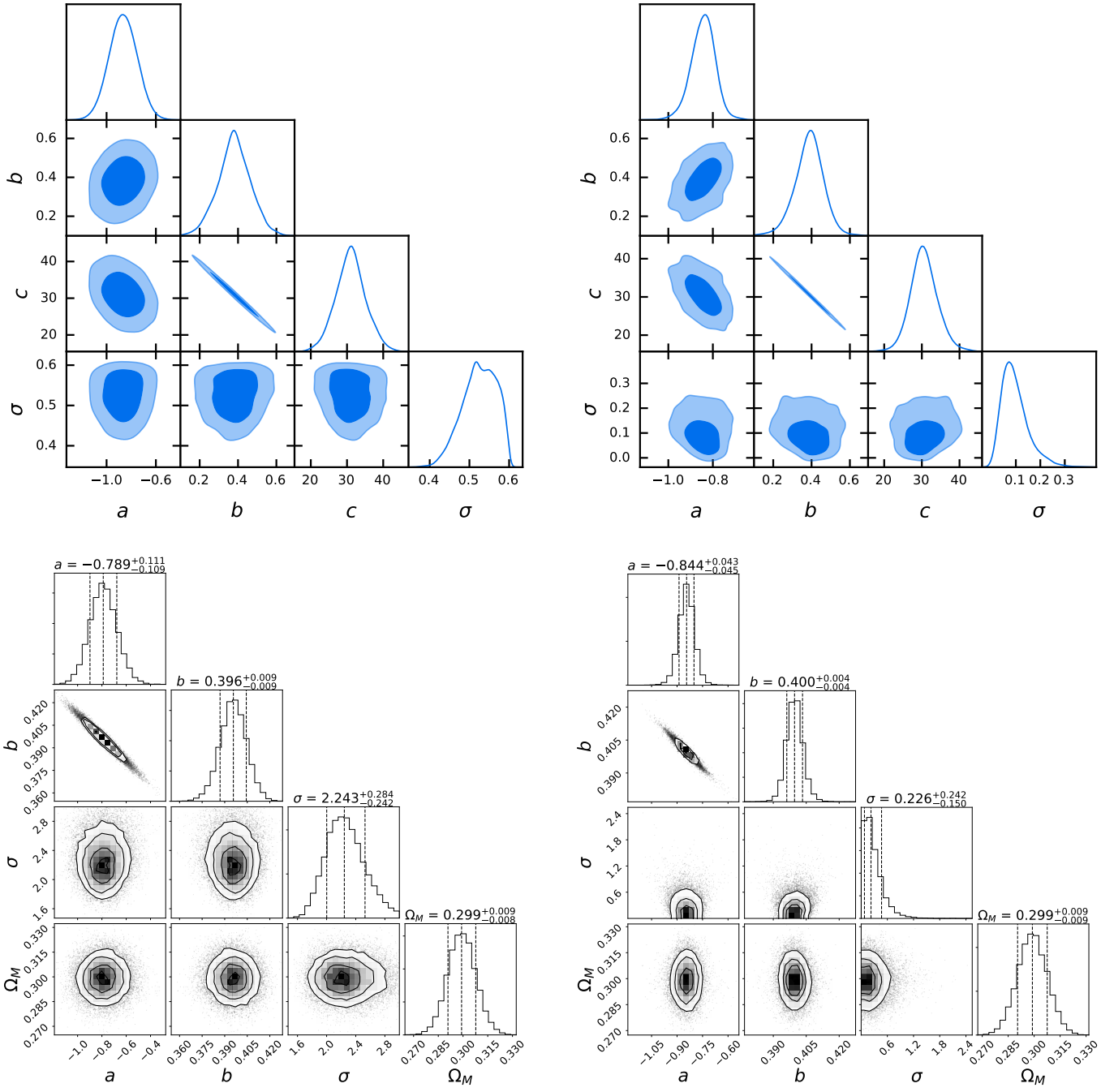

Figure 2. The upper panels show the fundamental plane fitting for the full GRB OPT sample (upper left) and the OPTtrim (upper right) calculated with *cobaya*. The bottom panels show the derivation of the Ω_M correspondent to the upper panels by the SNe Ia combined with both the full optical and the trimmed optical sample. Each plot shows the 2D posterior contours.

note in Table 2 that the error bars derived by the optical emission data is comparable with that of the X-ray sample, asserting that optical GRB data can be just as serviceable as X-ray ones in constraining cosmological parameters. Therefore, we continue the computations considering both wavelengths independently.

5 CONSIDERING REDSHIFT EVOLUTION CORRECTION

In this section, we perform the same analysis on all the combinations of samples studied in the previous sections, although now we account for redshift evolutionary effects. Because we deal with astronomical objects observed at large distances ($z \geq 0.033$), and because there also exists a dependence between GRB luminosity and redshift, we are aware of the data truncation due to the Malmquist bias and the Eddington effect (Eddington 1913; Malmquist 1922). To correct for these, we employ techniques as described by the Efron & Petrosian (1992) methodology on the full sample of 222 GRBs presenting X-ray plateaus. The EP method allows us to overcome the problems of redshift evolution and selection biases by introducing a modification of the Kendall rank correlation coefficient. This coefficient can be written in the following way:

$$\tilde{\tau} = \frac{n_c - n_d}{\frac{1}{2}n(n-1)} \tag{12}$$

where n_c is the number concordant and n_d is the number discordant. The EP test statistic is a similar non-parametric test, but the main improvement it makes upon Kendall's $\tilde{\tau}$ (Kendall 1938) is that it can work with both one-sided or doubly truncated data. It is defined as follows:

$$\tau = \frac{\sum_i (R_i - E_i)}{\sqrt{\sum_i V_i}} \tag{13}$$

where E is the expectation value, V is the variance, and R is rank. In order to use the EP method, we need to define the associated sets for which we will calculate the τ values. On the other hand, the associated sets are defined given a limiting value of a particular distribution. In our case we have a 3-variate distribution among $L_{\rm peak}$, $T_{\rm a}^*$ and $L_{\rm a}$. Thus, we define limiting fluxes for $L_{\rm peak,X}$ and $L_{\rm a,X}$ in X-ray as $1.54 \cdot 10^{-8}$ and $1.5 \cdot 10^{-12}$ ergs s^{-1}, respectively, and for $L_{\rm peak,\,OPT}$ and $L_{\rm a,OPT}$ in the optical as $1.40 \cdot 10^{-12}$ and $1.50 \cdot 10^{-14}$ ergs s^{-1}, respectively. These limits have been chosen in a conservative way so that no more than the 10% of the total sample for each physical parameter is cut via the EP method. This allows us to compute the uncertainty of the evolutionary effects without affecting the statistical significance of the samples. Simulations in Dainotti et al. (2013b) have shown the reliability of this method. The distribution of the limiting fluxes in X-ray and optical are shown in the two uppermost plots of Figs. 3 and 4, respectively; the limiting times in X-rays and optical are shown in the lower plots of the same figures. Once we correct for redshift evolution, we define new variables for GRB luminosities and times. These are the de-evolved variables, indicated with $'$. We define $L^{'} = L_X/(1+z)^{g(z)}$, where $g(z) = (1+z)^k$ is the function that mimics the redshift evolution for the X-ray luminosity at the end of the plateau emission. The same procedure has been applied for the peak luminosity in the prompt emission and for the time at the end of the prompt emission. The value of the exponent k is determined by the EP method (right panels of Figs. 3 for X-rays and 4 for optical). With the new evolutionary functions computed, we can then write the corrected by redshift evolution and selection bias fundamental plane relation:

$$\log_{10}(L_{\rm a,theory}) = c + a \times (\log_{10}(T_{\rm a}^*) - \log_{10}((1+z)^{k_{T_{\rm a}^*}})) + b \times (\log_{10}(L_{\rm peak}) - \log_{10}((1+z)^{k_{L_{\rm peak}}})) + \log_{10}((1+z)^{k_{L_{\rm a}}}) \tag{14}$$

so that $L_{\rm a}^{'}$, $L_{\rm peak}^{'}$, and $T_{\rm a}^{*'}$ become independent of redshift. Here, the k-corrections derived by the EP methodology for both X-ray and optical samples are defined in Table 3.

The fundamental plane fitting for the full OPT GRB sample, including evolution correction, produces the following parameters: $a_{\rm OPT,ev} = -0.74 \pm 0.11$, $b_{\rm OPT,ev} = 0.22 \pm 0.08$, $c_{\rm OPT,ev} = 37.52 \pm 3.78$ and $\sigma_{\rm int_{OPT,ev}} = 0.41 \pm 0.06$. When we consider the optical trimmed sample with evolution the parameters are the following: $a_{\rm OPT,trim,ev} = -0.77 \pm 0.15$, $b_{\rm OPT,trim,ev} = 0.22 \pm 0.15$, $c_{\rm OPT,trim,\,ev} = 37.61 \pm 2.97$, $\sigma_{\rm int_{OPT,trim,ev}} = 0.13 \pm 0.12$. Furthermore, we compute the plane fitting for the full X-ray GRB sample with evolution corrections and find the following: $a_{\rm X,PLAT,ev} = -0.85 \pm 0.12$, $b_{\rm X,PLAT,ev} = 0.48 \pm 0.12$, $c_{\rm X,PLAT,ev} = 25.64 \pm 6.55$ and $\sigma_{\rm int_{X,PLAT,ev}} = 0.20 \pm 0.06$. The X-rays trimmed and corrected with evolution has the following parameters: $a_{\rm X,trim,ev} = -0.79 \pm 0.17$, $b_{\rm X,trim,ev} = 0.49 \pm 0.19$, $c_{\rm X,trim,ev} = 25.29 \pm 9.87$ and $\sigma_{\rm int_{X,trim,ev}} = 0.13 \pm 0.09$. The percentage decrease regarding $\sigma_{\rm int_{X,trim,ev}}$ for the OPT sample considering the evolutionary effects is 68%, while for the X-ray one is 35%. It is interesting to note that the coefficient of the X-ray planes and the scatter results shown here, for which the most updated sample has been used, are within the $\sigma_{\rm int} = 0.22 \pm 0.10$ presented in Dainotti et al. (2020a).

All evolution-corrected results are displayed in Table 4 for comparison and some of the results for the full platinum and the optical samples and for their respective trimmed samples are shown in Fig. 5 . We note that they are very similar to the ones without correction; this could be due to the fact that the results with evolution carry a larger uncertainty on the variables, and this may lead to comparable results. More GRB data must be gathered so that the corrections for selection biases and redshift

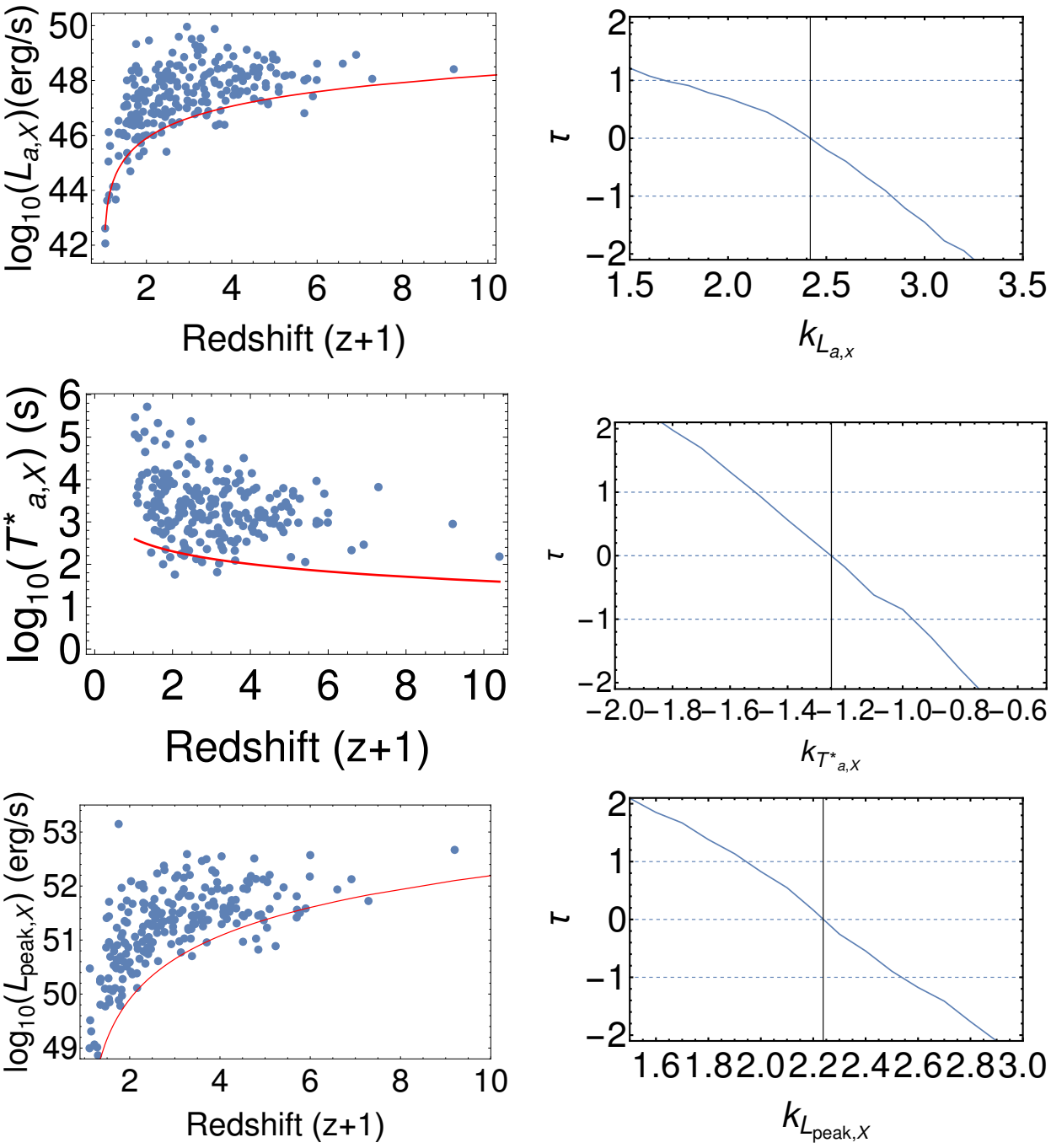

Figure 3. This figure shows how the limiting luminosities and the Kendall τ vs the slope of the evolutionary functions for the full X-ray GRB sample. The panels show the evolution of $L_{\rm a,X}$, $T^*_{\rm a,X}$, and $L_{\rm peak,X}$ vs. redshift. The limiting line is plotted in red. The right panels show the evolution of τ. The middle dashed line is $\tau = 0$ and the dashed lines are the defined bounds of $+1\sigma$ and -1σ, while the red line corresponds to the best-fit value of τ.

evolution carry less uncertainty. Thus, in the following sections when we consider the simulated data, we limit ourselves to the non-evolutionary cases.

6 SIMULATING GRBS FROM THE FULL SAMPLE FUNDAMENTAL PLANES

We now use the 3D fundamental planes in X-ray as defined by the 50 GRBs of the PLAT sample, and in optical (all 45 GRBs) as a base for simulating GRB events. We first perform these simulations to compute the number of GRBs in X-rays needed to achieve closed-contours around the mean value computed for $\Omega_{\rm M}$, without requiring any upper limit on the error. We begin by simulating Gaussian distributions resembling the observed $T^*_{\rm a,X}$, $L_{\rm a,X}$, and $L_{\rm peak,X}$, and the K-correction distributions from all

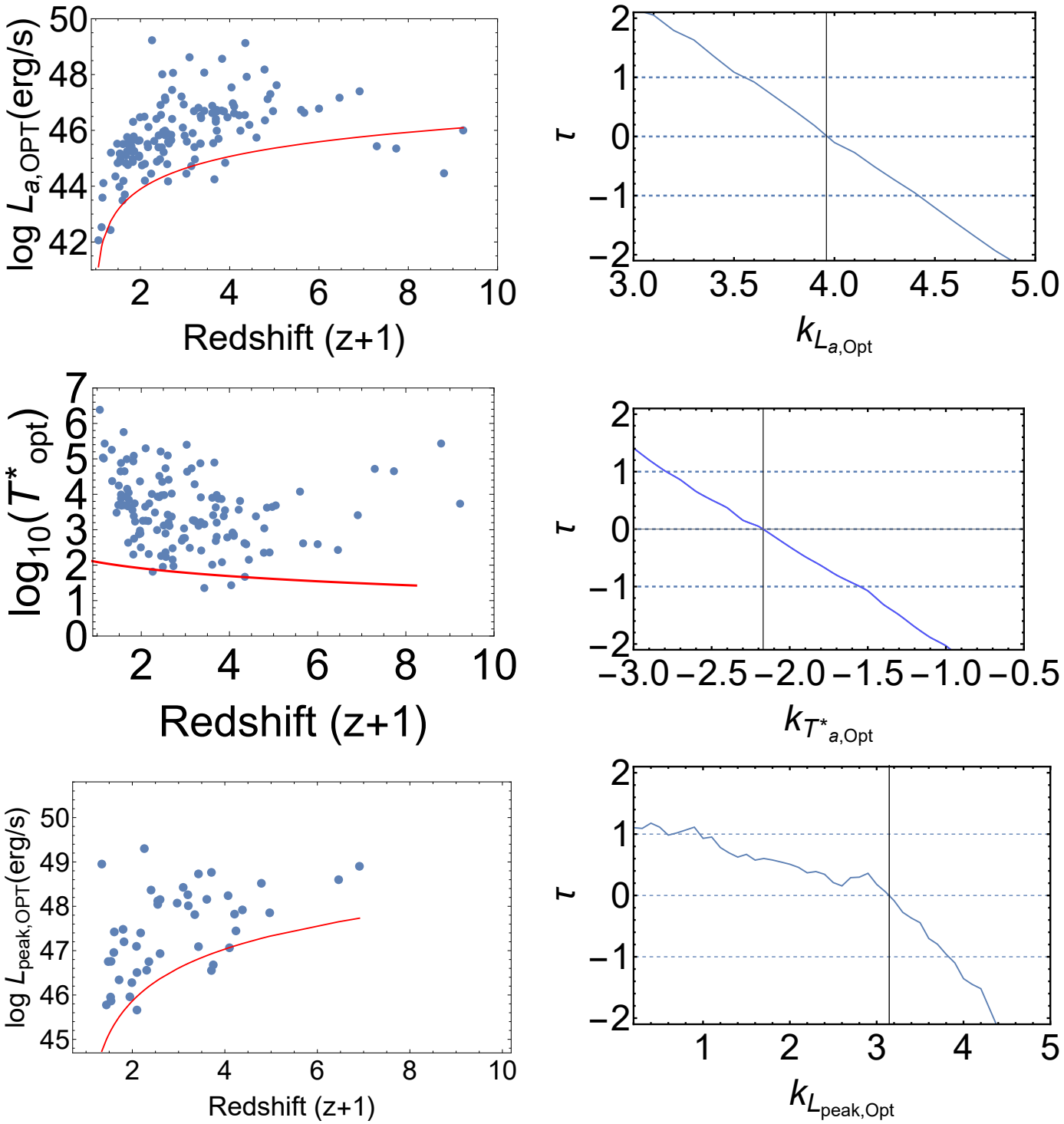

Figure 4. This Figure shows how the limiting luminosities and the Kendall τ vs the slope of the evolutionary functions for the full optical GRB sample. The panels show the evolution of $L_{a,OPT}$, $T^*_{a,OPT}$, and $L_{peak,OPT}$ vs. redshift. The limiting line is plotted in red. The right panels show the evolution of τ. The middle dashed line is $\tau = 0$ and the dashed lines are the defined bounds of $+1\sigma$ and -1σ, while the red line corresponds to the best-fit value of τ.

GRBs belonging to the PLAT X-ray fundamental plane. The errors on all of these variables have also been simulated in this way. We run this data through python's MCMC sampler *emcee* (Foreman-Mackey et al. 2013) to randomly simulate different numbers of GRBs. The *emcee* sampler has been chosen for simulation production due to its ease of parallelization over *cobaya*. We find that only 150 GRBs are needed to provide a reasonable Ω_M value of 0.387 ± 0.473, as shown in bottom left of Fig. 6. However, the error bars on this value are undesirable; much greater accuracy has been achieved by using SNe Ia as sole probes. We define three desired error limits as those determined by SNe Ia data as a standalone standard candle; Conley et al. (2011) determined a

Table 3. The table shows the coefficient of evolutionary functions for the luminosity at the end of the plateau emission, L_a, its correspondent rest frame, T_a^* and the peak prompt luminosity, L_{peak} for both X-ray (first row) and optical (second row).

Sample	kL_a	kT_a^*	kL_{peak}
X-ray	2.42 ± 0.58	-1.25 ± 0.28	2.24 ± 0.30
Optical	3.96 ± 0.43	-2.11 ± 0.49	3.10 ± 1.60

Table 4. The first column shows the evolution-corrected sample, while the second shows the correspondent values of Ω_M. The errors reported here are variances, corresponding to the 68% confidence limit.

Sample	Ω_M
PLAT+SNe Ia (EV)	0.299 ± 0.009
PLATtrim+SNe Ia (EV)	0.299 ± 0.008
OPT+SNe Ia (EV)	0.299 ± 0.008
OPTtrim+SNe Ia (EV)	0.299 ± 0.009

symmetrized error of $\sigma = 0.10$ from 472 SNe Ia, Betoule et al. (2014) obtained a standard deviation of $\sigma = 0.042$ from 740 SNe Ia, and Scolnic et al. (2018) obtained a standard deviation of $\sigma = 0.022$ from 1048 SNe Ia. The goal with simulating differently trimmed data is to reach a value for the error that is less than or equal to these error limits using GRBs as a standalone probe. We then use the number of GRBs needed to achieve this to infer the number of years needed, given present and future deep-space survey missions, to make this constraint possible. We start by choosing the errors found by Conley et al. (2011), because it has a sample size of SNe Ia more comparable to our sample size of 222 GRBs than other, more recent studies. Thus, we explore methods of reaching this error limit first by increasing the number of simulated GRBs off of the full PLAT sample, and then in the following subsections, trimming our PLAT sample to reach SNe Ia accuracies and define the smallest error on Ω_M yet.

Using all 50 PLAT GRBs in X-ray as the simulation base first, we test for a large range of simulated GRBs. We ran multiple simulations to see what it is the optimal number of GRBs simulated to increase the precision on our cosmological computation until the desired error limit is reached. We note the convergence of the Ω_M parameter to a value about 0.3 (see Fig. 7a), as expected. However, we also change the errors on the simulated $L_{a,X}$, $T^*_{a,X}$, and $L_{peak,X}$ to test simulated samples of varying quality. The first simulations were run by considering the original errors, and then halving those, resulting in increasingly better quality samples. As predicted, the samples simulated from the GRBs with halved error bars show a convergence to an Ω_M value with smaller standard deviations, see Fig. 7b, than those with undivided errors, as seen in Fig. 7a. In comparison to the previously stated Ω_M value for a sample of 150 simulated n = 1 GRBs, for the same-sized sample of 150 simulated n = 2 GRBs, we now achieve $\Omega_M = 0.416 \pm 0.177$. This represents a near 63% decrease on the error in Ω_M.

We constructed a probability map on the value of Ω_M as computed by the simulations. This was created by taking the Monte Carlo chains and computing the probability density function (PDF) on each simulation, and then converting this density to a probability. The PDFs were then linearly interpolated in the three-dimensional space of the number of GRBs, Ω_M, and the probability density from each simulation run to create a probability map. As is evident from Fig. 7c, we see no highly probabilistic closed contours for a number of GRBs less than 2100. However, if we are to focus our attention only on achieving the desired precision of Conley et al. (2011) of $\sigma = 0.10$, we reach this goal considering 789 GRBs. This error limit is represented by the bright green line in the left panel of Fig. 8. Thus, we can focus on the plots that show the error on Ω_M versus the correspondent number of simulated GRBs rather than Ω_M itself. 789 GRBs are needed to be able to use them as standalone standard candles when the errors that enter the likelihood remain undivided. Further, the grey line in the left panel of Fig. 8 shows that the Betoule et al. (2014) limit is reached for a minimum of 2653 simulated GRBs. The Scolnic et al. (2018) limit shown by the black line in Fig. 8 is not reached if we limit to a maximum number of 3000 GRBs.

Considering now the predictions if the errors are divided by two (Fig. 7b), we build a new probability map and observe the minimum width in the distribution, corresponding to the probability peak, beginning at around 2100 GRBs (Fig. 7d). We here stress that the above mentioned width of the distribution is correlated with the normalized standard deviation we see in the upper panels of Fig. 7. It should be noted that PDFs for both maps in the lower two panels of Fig. 7 are normalized with respect only to the simulations used in each respective map. What is important in the comparison between the two maps is the spread of the PDF for the number of GRBs that give the most probabilistic value for Ω_M. For the map of Fig. 7c (n = 1), the standard deviation on the normalized PDF of Ω_M is calculated as $\sigma_{pdf} = 0.037$, whereas the map of Fig. 7d (n = 2), it is correspondent to $\sigma_{pdf} = 0.022$. When the errors are halved, the Ω_M values present a smaller uncertainty, for a smaller number of simulated GRBs. Although this result is expected, we nevertheless perform simulations to investigate to which extent the number of GRBs needed to achieve the desired uncertainty on Ω_M is reduced as much as possible without the need of a relatively great increase

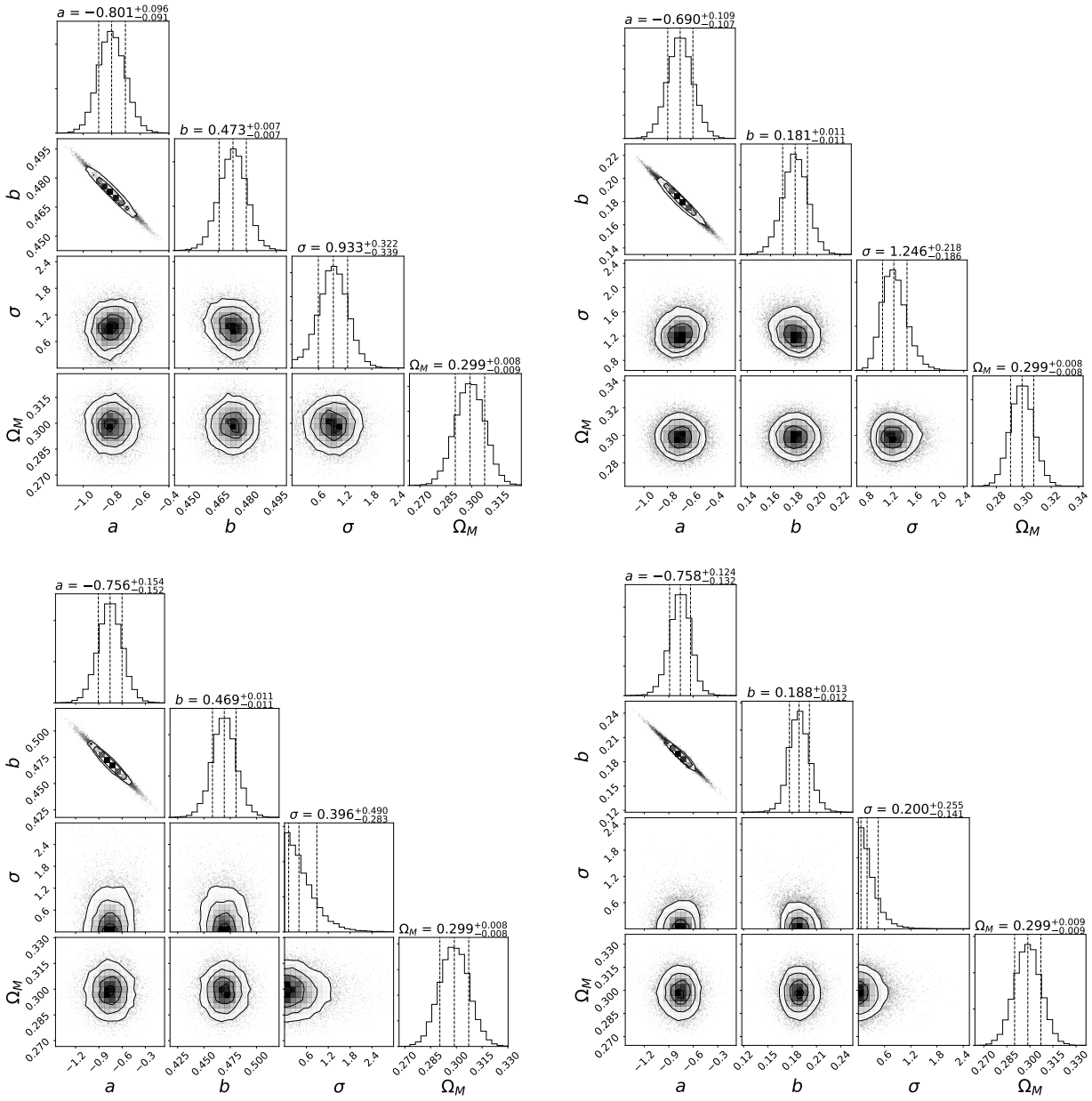

Figure 5. The upper panels show the fundamental plane fitting for the full GRB PLAT sample (upper left) and the OPT sample (upper right) with evolution performed contemporaneously with SNe Ia to derive the Ω_M values. The bottom panels show the same derivation of Ω_M with both the PLAT and optical trimmed samples (left and right panel, respectively). Each plot shows the 2D posterior contours as well as the 1D histograms for each parameter.

in the initial number of GRBs observed. Moreover, it is also important to note from Fig. 7 that the probability increases and, thus, the standard deviation decreases consistently for Ω_M values approaching 0.30. Specifically, for undivided errors, the most probable value is for $\Omega_M = 0.308 \pm 0.042$ at 2700 GRBs, and for halved errors, $\Omega_M = 0.300 \pm 0.027$ at 2600 GRBs. Furthermore and as expected, as the errors that enter the likelihood decrease, the number of GRBs needed to reach an Ω_M with the required accuracy also decreases. We again recover a lower number of GRBs needed if we look only to the number that falls under the $\sigma = 0.10$ error cutoff. All of the simulations we ran for halved errors had symmetrized errors below this error limit (see Fig. 8). As for the Betoule et al. (2014) limit, Fig. 8 shows that we reach a $\sigma = 0.042$ for 1452 GRBs. We here stress that in Fig. 8, as in the following ones with the exception of the figures in the Appendix, we obtain the limiting numbers of GRBs by extrapolation the polynomial fitting functions which are of various order from order 4th to order 7th. Moreover, the Scolnic et al. (2018) limit is reached with 2724 simulated GRBs in X-ray. These studies have been completed for a number of GRB samples of varying quality as defined by the division of the errors that enter the likelihood equation; we present only the two most likely scenarios of unchanged errors and halved ones both for conciseness and probability of utility. It is reasonable to assume a sample this